

Stochastic Dynamics of Sea Surface Height Variability

PHILIP SURA

Department of Meteorology, The Florida State University, Tallahassee, Florida

SARAH T. GILLE

*Scripps Institution of Oceanography, University of California, San Diego,
La Jolla, California*

(Manuscript received 5 August 2009, in final form 20 January 2010)

ABSTRACT

Sea surface height anomalies measured by the Ocean Topography Experiment (TOPEX)/Poseidon satellite altimeter indicate high values of skewness and kurtosis. Except in a few regions, including the Gulf Stream, the Kuroshio Extension, and the Agulhas Retroflection, that display bimodal patterns of sea surface height variability, kurtosis is uniformly greater than 1.5 times the squared skewness minus an adjustment constant. This relationship differs substantially from what standard Gaussian or double-exponential noise would produce. However, it can be explained by a simple theory in which the noise is assumed to be multiplicative, meaning that a larger background state implies larger random noise elements. The existence of multiplicative noise can be anticipated from the equations of motion, if ocean dynamics are split into a slowly decorrelating deterministic component and a rapidly decorrelating contribution that is approximated as noise. Such a model raises the possibility of predicting the probabilities of extreme sea surface height anomalies from first physical principles and may provide a useful null hypothesis for non-Gaussian sea surface height variability.

1. Introduction

Extreme events are by definition rare, but they can have a significant impact on the oceanic or atmospheric circulation. Understanding extremes has become an important objective in climate variability research. An extreme event is most commonly defined in terms of the tail of the data's probability density function (PDF). Climate and weather risk assessment depends on knowing the detailed structure of the tails of PDFs. In statistical analyses, we often assume that observations will have Gaussian PDFs. However, geophysical systems are not necessarily Gaussian, and deviations from Gaussianity can shed light on the underlying dynamics. In recent years, new quantitative tools that make use of advanced stochastic theory have evolved to evaluate extreme events (i.e., infrequent events associated with non-Gaussian statistics) and the physics that govern these events (e.g., Peinke et al. 2004; Majda et al.

2008; Monahan 2004, 2006a,b; Sura 2003; Sura and Gille 2003; Sura et al. 2005, 2006; Sura and Newman 2008; Sura and Sardeshmukh 2008; Sardeshmukh and Sura 2009).

Here, we will apply stochastic theory to altimetric measurements of sea surface height (SSH) anomalies, essentially a measure of variability in dynamic topography (or geostrophic streamfunction). PDFs that have previously been derived from altimeter data have been shown to be non-Gaussian, both for SSH (e.g., Thompson and Demirov 2006) and for geostrophic velocities derived from the horizontal gradients of SSH (e.g., Llewellyn Smith and Gille 1998; Gille and Llewellyn Smith 2000; Isern-Fontanet et al. 2006). Because geostrophic velocities are derived by differencing SSH values, the PDFs of geostrophic velocities are expected to resemble PDFs of SSH, convolved with themselves. In this study, we will therefore focus on SSH as the more basic and fundamental quantity. So far, the study of non-Gaussian variability inferred from SSH has been largely empirical: most investigators have used observations or model output to estimate the PDFs of SSH, without probing the dynamical reasons for the shape of the PDFs. For example, Thompson and Demirov (2006) examined the skewness

Corresponding author address: Philip Sura, Department of Earth, Ocean and Atmospheric Science, The Florida State University, 1017 Academic Way, Tallahassee, FL 32306-4520.
E-mail: psura@fsu.edu

of SSH anomalies from gridded altimeter data, and they found that many ocean features, such as western boundary currents, could be identified in the skewness map. However, the authors did not provide a dynamical explanation of the observed non-Gaussian structures beyond a qualitative picture derived from a quasigeostrophic numerical model. This study attempts to start filling this gap by analyzing non-Gaussian sea surface height variability in a recently developed stochastic dynamical framework.

Within that framework, analyses of skewness and kurtosis in sea surface temperature (SST; Sura and Sardeshmukh 2008) and in atmospheric geopotential height and vorticity (Sardeshmukh and Sura 2009) showed a strong constraint on the non-Gaussianity of those variables: the (excess) kurtosis is everywhere equal to or larger than 1.5 times the squared skewness (minus an adjustment constant). Sura and Sardeshmukh (2008) and Sardeshmukh and Sura (2009) developed a dynamical theory from first principles that is in good agreement with the observed skewness–kurtosis links and other observed non-Gaussian properties, such as power-law PDFs. Here, we will find that similar relationships exist for altimetric measurements, indicating that stochastic dynamics are capable of explaining non-Gaussian SSH variability as well.

At first sight, it seems very likely that SSH and SST should be governed by similar stochastic dynamics, because surface quasigeostrophic (SQG) theory predicts that both quantities should resemble each other on oceanic mesoscales (approximately <400 km; e.g., Lapeyre and Klein 2006; Isern-Fontanet et al. 2008). For example, we might expect skewness maps of SSH and SST to be almost identical on scales of meandering boundary current systems, such as the Gulf Stream, with first baroclinic Rossby radii smaller than 400 km (note that the typical Rossby radius in the Gulf Stream system is about 50–100 km and the typical width of the Gulf Stream is of the same order). However, as we will see, a comparison of SSH and SST skewness maps in the Gulf Stream region shows that their spatial distributions are not identical on those scales. This implies that the non-Gaussian extremes of SSH and SST variability are driven by different physical processes, and we have no a priori reason to expect the higher-order (non-Gaussian) statistics of SSH and SST to be governed by similar dynamics. One key assumption relating SST to SSH anomalies within SQG theory is that SST anomalies should fully represent surface density anomalies at the base of the mixed layer. This assumption neglects near-surface ocean conditions, therefore limiting the applicability of SQG theory to mixed layer dynamics. In fact, Isern-Fontanet et al. (2008) recognize that further research is needed to explore the role of the mixed layer in linking SST and SSH anomalies through SQG theory.

The observational analyses presented here contribute a step in that direction by showing that the global statistics of non-Gaussian SSH variability are consistent with the recently developed stochastic framework. However, although both non-Gaussian SST and SSH variability are generally consistent with stochastic multiplicative noise dynamics, there are significant local differences in the parameters, giving rise to different skewness maps in, for example, the Gulf Stream region. This suggests that mesoscale processes in the mixed layer are important for non-Gaussian SST variability (consistent with Sura and Sardeshmukh 2008) and that the SQG assumption linking SSTs to density anomalies below the mixed layer are not generally valid under extreme (non-Gaussian) conditions.

Therefore, in the following we extend the earlier work on SSH to examine how we can use non-Gaussian statistics to gain an improved understanding of the physics and statistics governing ocean circulation and, in particular, variability. In fact, the detailed analyses of higher-order statistics such as skewness and kurtosis are becoming more common, because the intricate link between ocean dynamics and non-Gaussian statistics is being explored more closely. For example, kurtosis of potential has been recently linked to mixing barriers in the ocean (Hughes et al. 2010). Besides the more specific dynamical issues mentioned, a detailed understanding of non-Gaussian SSH variability is also important for testing whether an observed sea level rise or storm surge is due to a trend or natural non-Gaussian variability. The stochastic dynamical analyses presented here may provide a useful null hypothesis for non-Gaussian SSH variability.

The results from altimeter data are presented in section 2. In section 3, we present a stochastic theory of SSH variability that explains the observed skewness–kurtosis link. Section 4 provides a summary and discussion.

2. Observations: Description and statistical analysis

In this analysis, we consider SSH anomalies along the Ocean Topography Experiment (TOPEX)/Poseidon satellite altimeter ground tracks. We use Archiving, Validation, and Interpretation of Satellite Oceanographic data (AVISO) that are archived at regular 10-km intervals along satellite ground tracks, with standard tidal and atmospheric corrections applied. Here, we analyze data from 25 September 1992 through 11 August 2002, corresponding to the duration of the TOPEX/Poseidon mission along its original ground tracks. We subtract the time mean from each observation so that at each measurement point SSH anomalies have a zero mean.

TOPEX/Poseidon operated with a 9.9-day repeat pattern, so up to 364 observations were collected at each measurement point during the 10-yr mission. This is an

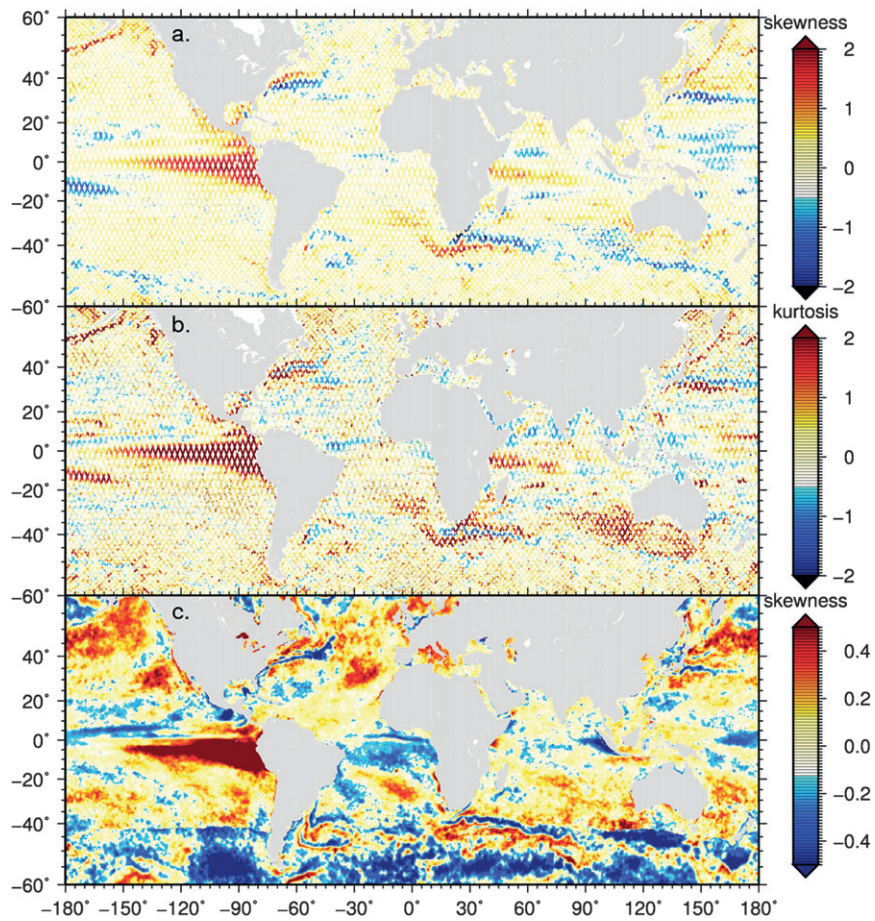


FIG. 1. (a) Skewness from TOPEX/Poseidon mission, computed for each data point along ground tracks. (b) Excess kurtosis, similarly computed along TOPEX/Poseidon ground tracks. (c) Skewness from SST anomalies, computed from daily Reynolds data, following Sura and Sardeshmukh (2008).

insufficient number of observations to compute a reliable PDF at each grid point. Previous research focused on PDFs has often binned data geographically to collect sufficient numbers of observations to assess PDFs reliably (e.g., Gille and Llewellyn Smith 2000; Gille 2004). However, binning data from distinctly different regions can alter PDFs. Instead of binning, here we first characterize the overall shape of the PDF using the skewness and the kurtosis of the data.

For SSH anomalies h' with zero mean and standard deviation σ , the skewness S and kurtosis K are defined as

$$S \equiv \frac{\overline{h'^3}}{\sigma^3} \quad \text{and} \quad (1)$$

$$K \equiv \frac{\overline{h'^4}}{\sigma^4} - 3, \quad (2)$$

where the overbar denotes a time average or, assuming ergodicity, an ensemble average. In the following

discussion, we can employ the notion of a time average in most of the cases. Skewness represents the asymmetry of the PDF. It is positive if the right tail contains more data than the left tail, and it is negative if the opposite is true. Symmetric distributions, such as the classic Gaussian, have zero skewness. Kurtosis represents the peakiness of the data distribution; it is high when the data include numerous extreme events. Our definition K here is sometimes referred to as “excess kurtosis,” because we have subtracted 3, corresponding to the kurtosis for a Gaussian distribution.

Figure 1a shows along-track skewness, and Fig. 1b shows along-track kurtosis of SSH. In some regions, the SSH maps show structures that resemble skewness and kurtosis maps produced for SST anomalies by Sura and Sardeshmukh (2008); see Fig. 1c for SST skewness. [To very briefly recapitulate, the SST dataset consists of a blended analysis of daily SST fields based on infrared satellite data from the Advanced Very High Resolution

Radiometer (AVHRR) and in situ data from ships and buoys (for details see Reynolds et al. 2007). The daily SST data are available on a 0.25° latitude-longitude grid from the early 1980s to the present. SST anomalies were calculated by subtracting the daily climatology and linear trend from the full daily values.] For example, large patches of SSH and SST skewness and kurtosis in the eastern tropical Pacific are related to El Niño–Southern Oscillation variability, which dominates the statistics of the region. In other regions, the maps differ on smaller spatial scales (<400 km) where SQG theory would predict skewness maps of SSH and SST to be almost identical (e.g., Lapeyre and Klein 2006; Isern-Fontanet et al. 2008). In dynamically active regions of meandering jets (with first baroclinic Rossby radii smaller than 400 km) such as the Gulf Stream, the Kuroshio Extension, and the Agulhas Retroflection, SSH skewness forms a dipole pattern, with negative values on equatorward sides of frontal features and positive values on poleward sides. As explained by Thompson and Demirov (2006), this structure is consistent with the fact that these fronts are meandering jets. In contrast, SST anomalies show a very different tripole pattern, with negative skewness in the mesoscale (or Rossby radius scale) core of the current, sandwiched between regions of positive skewness (for details, see Sura 2010). As a striking example, we compare SSH and SST skewness maps of the Gulf Stream region in Fig. 2. SST is shaded in Fig. 2a, and SSH is shaded in Fig. 2b. In both panels, green contours indicate SST and black contours indicate SSH. Note that the region of negative SST skewness almost exactly matches the Gulf Stream and therefore has a spatial scale on the order of the Rossby radius. This comparison of SSH and SST skewness in the Gulf Stream region shows that their spatial distributions are not identical on Rossby radius scales. In particular, along the Gulf Stream maximal negative SST skewness coincides with zero contours of SSH skewness. This implies that non-Gaussian extremes of SSH and SST variability are driven by different physical processes, and we have no a priori reason to expect the higher-order (non-Gaussian) statistics of SSH and SST to be governed by similar dynamics. Other differences emerge in the Southern Ocean and Northern Hemisphere subtropical gyres, where SST variability shows large-scale patterns of skewness and kurtosis that do not emerge in SSH, which is governed by local processes related to geostrophic flow. Finally, note also the very different patterns in the tropical Indian Ocean.

Because SSH and SST statistics differ in large parts of the ocean on large scales and particularly mesoscales (where SQG theory applies), we have to conclude that SSH and SST are not necessarily interchangeable proxies of each other for large-amplitude (non-Gaussian) oceanic

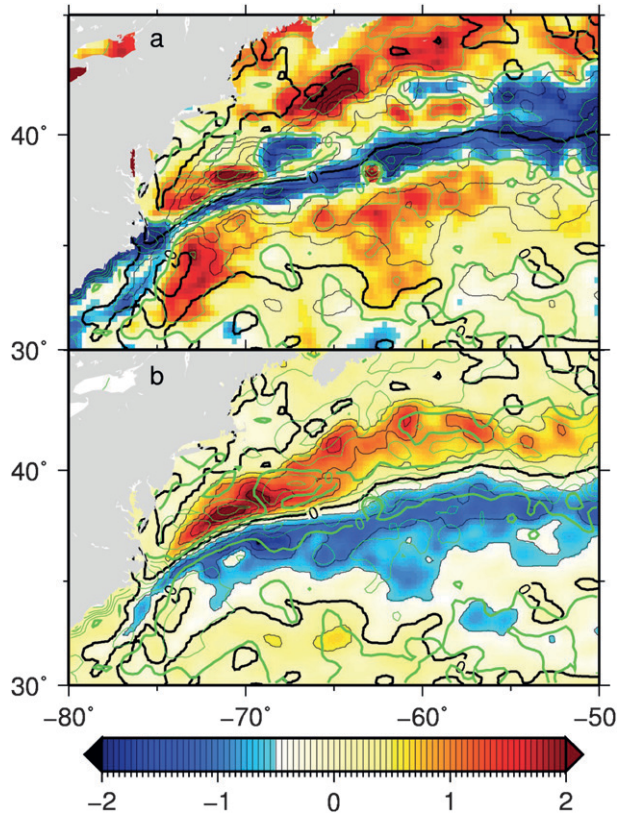


FIG. 2. (a) Inset of SST skewness from daily Reynolds data for the Gulf Stream region (shaded). (b) SSH skewness from AVISO altimetry for the same region (shaded). In both cases, green contours indicate SST and black contours indicate SSH.

mesoscale phenomena. This suggests that some processes in the mixed layer are important for non-Gaussian SST variability (consistent with Sura and Sardeshmukh 2008) and that the SQG assumption linking SSTs to density anomalies below the mixed layer may not be generally valid under extreme (non-Gaussian) conditions. Therefore, in this paper, we will pursue an independent study of the physics underlying non-Gaussian SSH variability.

The key to understanding the dynamics of non-Gaussian SSH anomalies lies in the link between skewness and kurtosis, as we will show in section 3. Formally, for data drawn from any PDF, the skewness sets a lower bound on the size of the excess kurtosis K (e.g., Wilkins 1944):

$$K \geq S^2 - 2. \quad (3)$$

Here, we find that kurtosis is between ± 2 over large regions of the ocean, implying moderate non-Gaussian variability. Places where kurtosis significantly exceeds 2, along the equatorial Pacific and in regions of strong western boundary currents, are also regions with significant nonzero skewness. High kurtosis indicates large

numbers of extreme events, which might, for example, be associated with rare but strong eddy events. Even a system with essentially Gaussian PDFs can exhibit high kurtosis, if it switches over time between low and high variance conditions (i.e., if the width of the PDF can change). Thus, the high kurtosis in the eastern tropical Pacific can be attributed to the extreme (40 cm) SSH anomalies observed during the 1997/98 El Niño event. If data from that time period are removed, kurtosis drops from values around 4 or 5 to values in the range ± 2 .

Because skewness and kurtosis are sensitive to outliers, they could potentially be biased by measurement problems. Gille and Llewellyn Smith (2000) were reluctant to interpret geostrophic velocity PDF tails for this reason, and their analysis focused on the fact that the cores of velocity PDFs are essentially Gaussian in most geographic regions. In fact, closer inspection suggests that geostrophic velocity PDFs from altimetry closely resemble in situ velocity PDFs [see, e.g., results of Bracco et al. (2000) and LaCasce (2005)]. In both cases, the PDFs have Gaussian cores but non-Gaussian tails. PDFs for SSHs or dynamic topography are expected to show similar patterns; therefore, here we have included the observed tails in our analysis.

In contrast with Thompson and Demirov (2006), who based their work on gridded AVISO (Ducet et al. 2000), here we present result derived from ungridded along-track SSH data. Both gridded and along-track data have specific advantages and disadvantages. Gridded data are easy to analyze, and the mapping procedure used to grid data provides a means to remove outliers that might result from unphysical instrumental error. On the other hand, if outliers represent true physical events, then along-track data are preferable. Because we do not have a noise-free measure of truth, there is no easy way to judge whether gridded or along-track data provide a better indication of the true PDFs. To evaluate possible biases, we separated the gridded data into two groups: points that fell along TOPEX/Poseidon ground tracks versus points that were distant from a ground track. We found statistically significant differences in the skewness and kurtosis between the two groups, with smaller kurtosis (implying more Gaussian statistics) for off-track data than for along-track data. Because this suggests that biases might be introduced by the gridding procedure, here we report values based on along-track data. However, the distinctions are minor; we have also carried out our calculations using gridded AVISO, and we find that the core results are essentially identical.

The exact standard errors of skewness and kurtosis depend on their underlying population distribution but can be approximated using a Gaussian as $\sigma_s = \sqrt{6/N_{\text{in}}}$ and $\sigma_k = \sqrt{24/N_{\text{in}}}$ respectively, where N_{in} is the effective

number of independent observations (e.g., Brooks and Carruthers 1953). In general, uncertainties can be expected to be smaller for PDFs with low kurtosis and higher for PDFs with high kurtosis. Here, we use the common error bars based on a Gaussian distribution, but note that they may underestimate true uncertainties by more than a factor of 2 in places where PDFs are highly non-Gaussian. On the other hand, the local error estimates ignore the spatial coherence of the moments. That is, if we see large coherent regions in the geographical maps of the moments, we may trust them even if they do not satisfy local significance criteria.

How do we use a link between skewness and kurtosis to interpret non-Gaussian ocean dynamics? Rather than focusing on the detailed dynamics of SSH at a given location, we are primarily interested in a global view of non-Gaussian SSH variability and in the global dynamical constraints induced by local dynamics. As we will discuss in the remainder of this paper, the functional form of the skewness–kurtosis relationship gives us a tool to study links between local and global SSH dynamics and will reveal fundamental dynamical principles governing non-Gaussian SSH variability.

Although (3) sets a general constraint for unimodal distributions (i.e., distributions with a single peak) such as SSH in most parts of the ocean,

$$K \geq S^2 - 186/125 \approx S^2 - 1.5 \quad (4)$$

(Klaassen et al. 2000). Figure 3 shows a scatterplot of skewness versus kurtosis for all shown in Fig. 1; the estimated local standard errors are indicated as well. The dotted and dashed lines in Fig. 3 indicate theoretical lower bounds for kurtosis. The observations substantially exceed these formal limits, and the solid gray line shows a lower bound on excess kurtosis in our dataset, which we find empirically to be

$$K > 1.5S^2 - 1.5. \quad (5)$$

Thus, the observations usually appear to be governed by a stronger lower bound than the formal statistical limit defined by (4).

For reference, Fig. 4 shows expected skewness–kurtosis relationships for three different standard PDFs. The uniform PDF values (top panel) cluster near the formal lower bound. Gaussian PDF values (middle panel) are distinctly different from the lower bound curves but do not show any examples of high skewness or high kurtosis. Double-exponential PDFs (bottom panel) are more strongly separated from the lower bound curves than the observations and have a slightly parabolic distribution reminiscent of the observations shown in Fig. 3. However, the

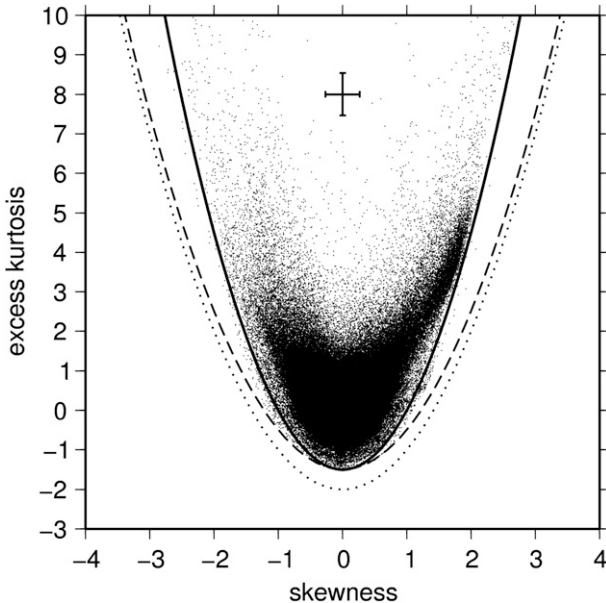


FIG. 3. Scatterplot of skewness vs excess kurtosis for SSHs measured by the TOPEX/Poseidon mission. Dots come from all latitudes and longitudes but are only plotted if more than 300 observations are available. The dotted line indicates the theoretical lower bound for any PDF, the dashed line indicates the theoretical lower bound for a unimodal PDF, and the solid line corresponds to $K = (3/2)S^2 - 1.5$. The error bars near the top denote the standard errors in K and S .

observations in Fig. 3 indicate many more high skewness and high kurtosis examples than any of these three theoretical PDFs would suggest, implying that SSHs do not conform to those standard PDFs.

The observed skewness–kurtosis relationship varies with latitude, as indicated in Fig. 5, which shows the data sorted into 10° wide latitude bands. Kurtosis is close to the formal lower bounds at midlatitudes (between about 30° and 50° latitude). In contrast, at high latitudes (50° – 60° S and 50° – 60° N) and to a lesser extent in the tropics, the scatterplot shows a large white band with no observations between the plotted curves and the lowest kurtosis values. The observed white bands are not as wide as the lower panel of Fig. 4 suggests for a double-exponential PDF but are consistent with what is expected for observed PDFs having a Gaussian core and non-Gaussian tails (e.g., Bracco et al. 2000; Gille and Llewellyn Smith 2000; LaCasce 2005). This suggests that the lower bound on kurtosis depends on geographically varying processes.

To probe the origins of this geographic variation, we identified points with unusually low K , relative to $1.5S^2 - 1.5$. Of more than 485 000 total observation points, just 658 had values of kurtosis low enough to violate $1.5S^2 - 1.5$. These are indicated with red dots in

Fig. 6. They occur in clusters in the Gulf Stream, in the Kuroshio and its extension, in the Gulf of Mexico Loop Current, in the Agulhas Retroflexion, and at a few points in the eastern tropical Pacific.¹ Low values of kurtosis, for which $K < 1.5S^2 - 1.3$, (blue points) occur in the same regions as the red clusters of points. All of these regions are marked by strong variability. A number of studies have reported bimodal patterns of variability in western boundary current regions (e.g., Bane and Dewar 1988; Chao 1984; Qiu and Miao 2000; Schmeits and Dijkstra 2001; Dong and Kelly 2004). Similarly, the Loop Current can be thought of as showing a bimodal behavior that depends on its penetration into the Gulf of Mexico (e.g., Maul and Vukovich 1993; Sturges and Leben 2000). Figure 7 shows that all four of these regions show evidence for bimodal sea surface height PDFs. Bimodal PDFs are not expected to conform to (4); thus, the bimodality appears likely to explain the low values of K that appear in these areas. Because the western boundary current regions are located between 30° and 50° latitude, they account for the particularly low values of K seen in Fig. 5 in these latitude ranges. Sea surface height in the eastern tropical Pacific is less clearly bimodal, but it exhibits some elements of bimodal behavior depending on the phase of El Niño–Southern Oscillation.

To evaluate the non-Gaussian structure of SSH variability in more detail, we also calculated PDFs for two representative regions within the ocean interior (Fig. 8) and two areas within the Agulhas region (Fig. 9). In the ocean interior, we contrast an area with weak positive skewness (interior I: 25.0° – 30.0° S, 350.0° – 360.0° E; Fig. 8a) against an area with strong negative skewness (interior II: 35.0° – 40.0° S, 320.0° – 330.0° E; Fig. 8b). In the Agulhas region, we compare an area with strong positive skewness (Agulhas I: 40.0° – 45.0° S, 10.0° – 20.0° E; Fig. 9a) to an area with strong negative skewness (Agulhas II: 34.8° – 36.5° S, 23.0° – 26.1° E; Fig. 9b). Height anomalies within each box are normalized by their standard deviation, and PDFs are plotted on log–log scales. In a log–log plot, a highly non-Gaussian power-law tail [i.e., a PDF $P(h') \propto h'^{-\alpha}$ with the exponent α] will appear as a straight line. Power laws play an important role in quantifying the probability of extreme events in many disciplines as diverse as physics, earth and planetary sciences, biology, economics and finance, computer science, and social sciences (e.g., Sornette 2006; Newman 2005). One important property of power laws is known as “self similarity” or “scale

¹ K is also low at a few isolated points along coastlines. We will not pursue these points because they may be due to errors in the nearshore tide model, coastal dynamics, or altimeter sampling problems along the coast.

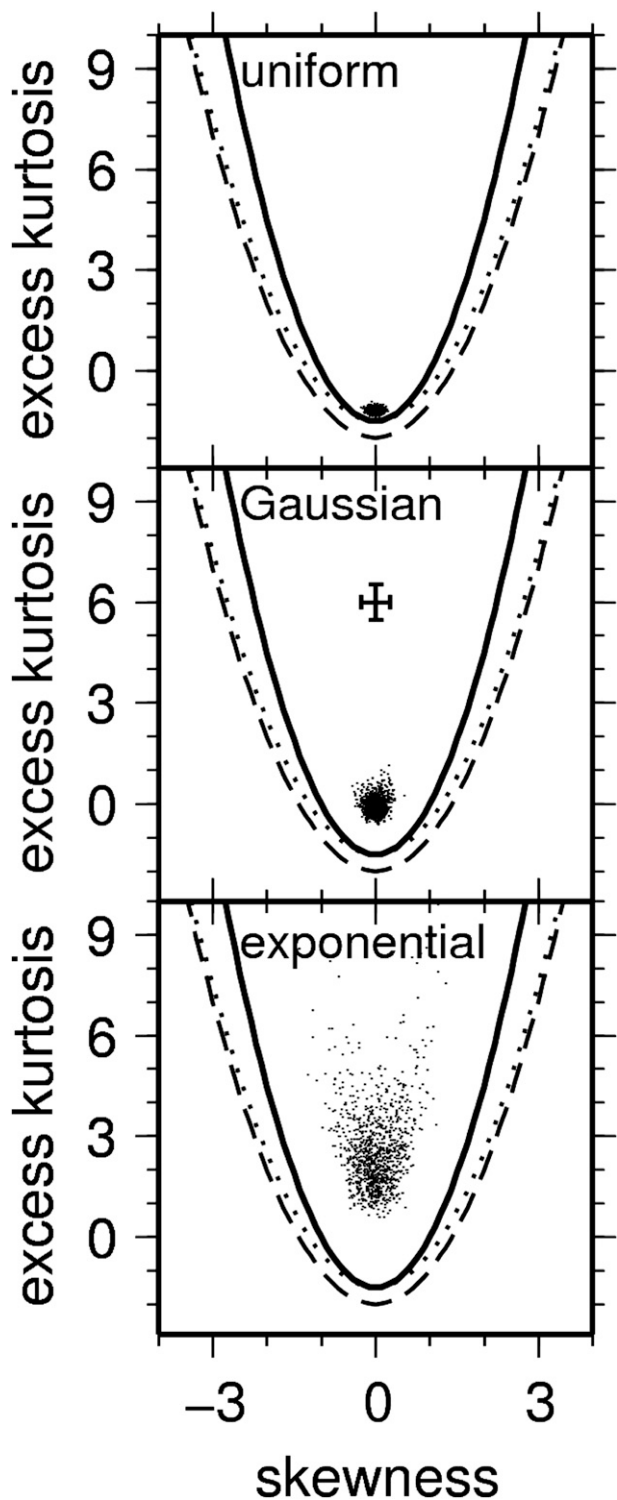


FIG. 4. Scatterplot of skewness vs excess kurtosis for 1000 random samples drawn from (top) a uniform distribution, (middle) a Gaussian distribution, and (bottom) a double-exponential distribution. Each skewness/kurtosis value is computed from 339 random points, corresponding roughly to the number of samples typically available at the TOPEX/Poseidon measurement points.

invariance": the ratio of any two probabilities $P(x_1)$ and $P(x_2)$ is only a function of the ratio x_1/x_2 ; $P(x_1)/P(x_2) = (x_1/x_2)^{-\alpha}$. This self-similarity is observed in many non-Gaussian natural phenomena, and we would like to see if non-Gaussian SSH anomalies follow a power law. Most important, as we will see later (in the next section), a power law in conjunction with the observed skewness–kurtosis link points to a specific physical process responsible for the extreme events.

In Figs. 8 and 9, positive normalized height anomalies h' are indicated by triangles and negative normalized h' are indicated by circles. Because the emphasis is on extreme events, the center of the PDF ($\pm 1\sigma$) is not shown. In fact, the center of the PDF is close to being Gaussian, consistent with previous studies of geostrophic velocities (e.g., Bracco et al. 2000; Gille and Llewellyn Smith 2000; LaCasce 2005). In all plots the solid line denotes a Gaussian distribution. The straight dashed lines are maximum likelihood estimates of the power-law behavior (given by the exponent α) above a systematically estimated lower bound $|h'|_{\min}$. A brief review of how to estimate power-law exponents from data can be found in the appendix [for details, see Newman (2005) and Clauset et al. (2009)]. The tails decay linearly in large regions of the PDF domain, providing compelling evidence for power-law behavior of SSH variability. However, the power-law scaling is not constant throughout the PDF domain but instead shows an approximately piecewise linear behavior (in log–log coordinates). That means that the PDFs show a different scaling above a certain value of h' (a scale break) in some PDFs. Nevertheless, in all cases, the power-law behavior above a scale break is statistically significant as tested by Kolmogorov–Smirnov statistics (see Newman 2005; Clauset et al. 2009). The different scalings may point to mechanisms not included in our simple model.

3. Origins of the observed K–S relationship and power-law scaling

In section 2, we found that simple statistical arguments alone are insufficient to explain the observed usual open ocean relationship between skewness and kurtosis of SSH anomalies, $K \geq 1.5S^2 - 1.5$, that is shown in Fig. 3. Neither a Gaussian nor an exponential PDF would be expected to produce the relationships seen in our data. We also provided evidence that SSH anomalies follow an approximately piecewise power-law distribution. Therefore, in this section we investigate whether dynamical processes can provide additional insight into the behavior in regions where PDFs are expected to be unimodal. We will specifically examine the impact of noise on creating the non-Gaussian features observed in SSH. Note that

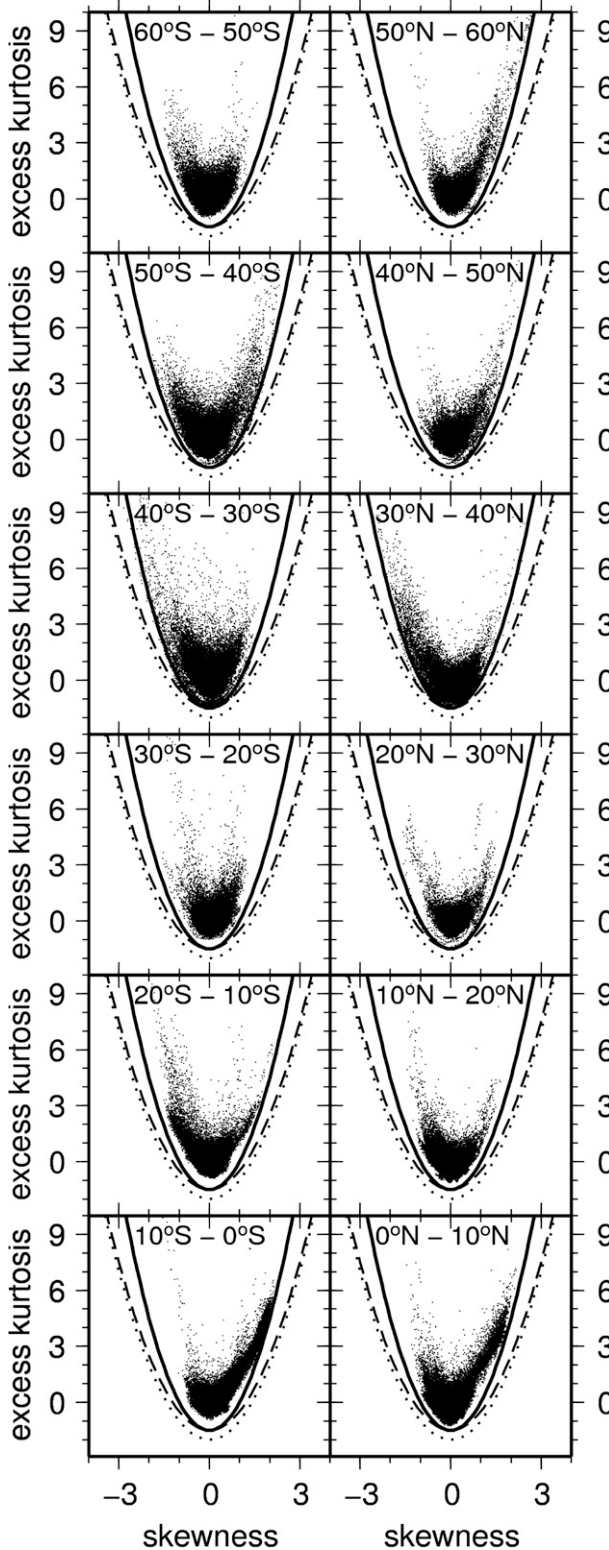


FIG. 5. Scatterplot of skewness vs excess kurtosis as in Fig. 3, but sorted as a function of latitude to show geographic variations.

the theory discussed later is not capable of reproducing multiple PDF maxima (or regimes) observed in some western boundary current regions (Fig. 7). Most likely, those maxima are related to localized multiple equilibria in the equations of motion, pointing to nonlinear processes on the spatial scale of the currents. The stochastic model discussed here certainly lacks the physical mechanism responsible for multiple regimes. Although this is a shortcoming of our approach, we have enough evidence to believe that the stochastic framework is indeed responsible for the power-law character of the observed PDFs. That is, we may think of a given PDF in an energetic, nonlinear boundary current as being composed of a stochastically forced power law plus a contribution from the multiple equilibria. Keep in mind, though, that the regions where multiple regimes are observed have very limited extent and that an undersampled power-law tail may also be interpreted as a distinct nonlinear regime.

The governing equations of fluid dynamics can be expressed in the general form (e.g., Salmon 1998)

$$\frac{dX_i}{dt} = L_{i,j}X_j + N_{i,j,k}X_jX_k + F_i, \quad (6)$$

where the state of the fluid is given by the vector \mathbf{X} with components X_i , and Einstein's summation convention is used. The first and second terms on the right are the linear and quadratically nonlinear tendencies (including linear and quadratically nonlinear damping terms), and F_i denotes a forcing term.

To see how we obtain such an abstract system, we consider, without loss of generality, the frictionless shallow-water equations for a fluid of total depth H ,

$$\frac{\partial \mathbf{u}}{\partial t} + \mathbf{u} \cdot \nabla \mathbf{u} + \mathbf{f} \times \mathbf{u} = -g \nabla H \quad \text{and} \quad (7)$$

$$\frac{\partial H}{\partial t} + \nabla \cdot (\mathbf{u}H) = 0, \quad (8)$$

where $\mathbf{u} = [u(x, y, t), v(x, y, t)]$ is the horizontal velocity vector and g is the acceleration of gravity. A spatial discretization or Fourier transformation of the equation of momentum (7) or continuity (8) will always yield an equation of type (6). Because we are interested in the dynamics at a given location, we will use spatial discretization to derive (6) from (7) and (8). We employ a simple nonstaggered grid with zonal index i and meridional index j , here using centered differences for illustrative purposes.²

² Centered differences can be numerically unstable, but our goal here is not to derive a numerically stable form of the equation but rather to motivate a form of the general Eq. (6) that can be used to interpret observations.

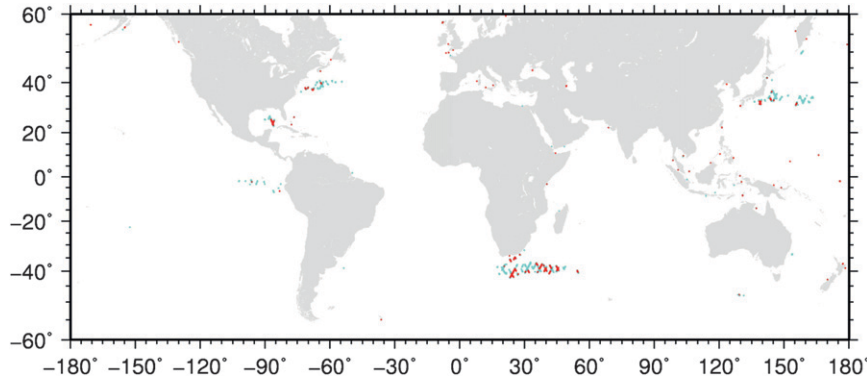


FIG. 6. Locations of low kurtosis, where either $K < 3/2S^2 - 1.3$ (blue dots) or $K < 3/2S^2 - 1.5$ (red dots). There are 658 red points and an additional 1159 points that are blue (but not red) out of a total of 485 502 observation points.

The spatial discretization yields

$$\begin{aligned} \frac{\partial u_{i,j}}{\partial t} + u_{i,j} \left(\frac{u_{i+1,j} - u_{i-1,j}}{2\Delta x} \right) + v_{i,j} \left(\frac{u_{i,j+1} - u_{i,j-1}}{2\Delta y} \right) - f v_{i,j} \\ = -g \left(\frac{H_{i+1,j} - H_{i-1,j}}{2\Delta x} \right) \end{aligned} \quad (9)$$

for the zonal momentum,

$$\begin{aligned} \frac{\partial v_{i,j}}{\partial t} + u_{i,j} \left(\frac{v_{i+1,j} - v_{i-1,j}}{2\Delta x} \right) + v_{i,j} \left(\frac{v_{i,j+1} - v_{i,j-1}}{2\Delta y} \right) + f u_{i,j} \\ = -g \left(\frac{H_{i,j+1} - H_{i,j-1}}{2\Delta y} \right) \end{aligned} \quad (10)$$

for the meridional momentum, and

$$\begin{aligned} \frac{\partial H_{i,j}}{\partial t} + \frac{u_{i+1,j} H_{i+1,j} - u_{i-1,j} H_{i-1,j}}{2\Delta x} \\ + \frac{v_{i,j+1} H_{i,j+1} - v_{i,j-1} H_{i,j-1}}{2\Delta y} = 0 \end{aligned} \quad (11)$$

for the continuity equation. It is obvious from (9)–(11) that a general equation of type (6) follows if we combine the variables $u_{i,j}$, $v_{i,j}$, and $H_{i,j}$ into a single vector X_i . Note that any finite-difference discretization will result in an equation of type (6). In addition, allowing vertical motion, adding friction, forcing, and including an advection equation for temperature and/or salinity does not change the general form of (6); only the definition of the vector component X_i and the coefficients $L_{i,j}$ and $N_{i,j,k}$ may change. A Fourier transformation or EOF decomposition of the governing equations of fluid dynamics will also result in the same type of generalized Eq. (6) (e.g., Salmon 1998). Thus, (6) represents an abstract form of the governing equations of fluid dynamics, and we may use it as a rigorous starting point for the following discussion.

The next step is to expand X_i in (6) into a mean and anomaly, $X_i = \bar{X}_i + X'_i$. Note that this is the usual Reynolds averaging procedure and that therefore the averaging period is not crucial for general form of the equations. For oceanic or climatological application, the mean could be defined as an annual or seasonal mean, or the mean seasonal cycle. The equation for the anomalies becomes

$$\begin{aligned} \frac{dX'_i}{dt} = [L_{i,j} + (N_{i,j,k} + N_{i,k,j})\bar{X}_k]X'_j \\ + N_{i,j,k}(X'_j X'_k - \bar{X}'_j \bar{X}'_k) + F'_i. \end{aligned} \quad (12)$$

Ocean (and atmospheric) dynamics can be split into a slowly decorrelating contribution and a rapidly decorrelating contribution. For example, the geostrophic component varies on much slower time scales than the ageostrophic motion. The (quasi) geostrophic approximation functions as a dynamically based low-pass filter (e.g., Pedlosky 1987; Salmon 1998) and was in fact originally developed for early weather forecast models with the intent to filter out all rapidly varying signals (such as gravity and inertio-gravity waves) to allow for much longer time steps and easier initializations (Lynch 2006). The decomposition into fast and slow modes is also a common approximation made in turbulence theory. Thus, we let \mathbf{X} consist of slow components \mathbf{x} and fast components \mathbf{y} , so that $\mathbf{X}^T = (\mathbf{x}^T \mathbf{y}^T)$ and $\bar{\mathbf{X}}^T = (\bar{\mathbf{x}}^T \bar{\mathbf{y}}^T)$. As in turbulence theory, the definitions of slow and fast are somewhat vague. For our purpose, it is sufficient to require that the fast motion decorrelates more rapidly than the slow motion (Hasselmann 1976). Thus, we can safely interpret the geostrophic component of the flow as the slow part and the ageostrophic component as the fast part. The equation for the slow anomaly becomes

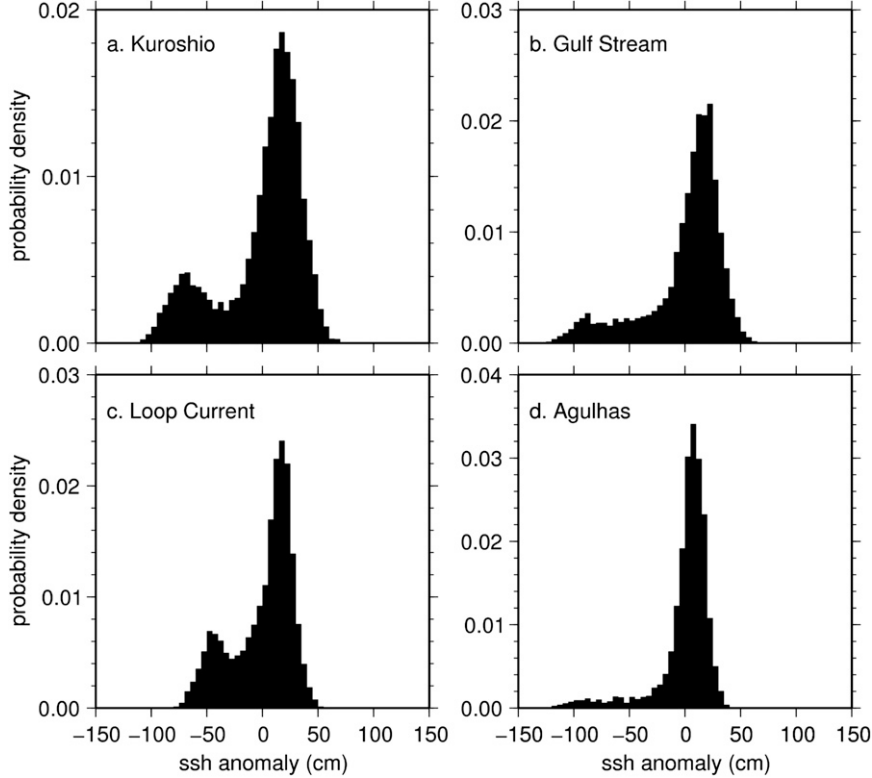


FIG. 7. PDFs for four regions identified in Fig. 6 having low kurtosis $K < 3/2S^2 - 1.5$; (a) Kuroshio: $31.6^\circ\text{--}33.1^\circ\text{N}$, $138.5^\circ\text{--}139.5^\circ\text{E}$; (b) Gulf Stream: $37.15^\circ\text{--}37.65^\circ\text{N}$, $291.6^\circ\text{--}292.4^\circ\text{E}$; (c) Loop Current: $23.0^\circ\text{--}25.7^\circ\text{N}$, $272.6^\circ\text{--}274.2^\circ\text{E}$; and (d) Agulhas: $36.5^\circ\text{--}35.7^\circ\text{S}$, $23.3^\circ\text{--}23.7^\circ\text{E}$.

$$\begin{aligned} \frac{dx'_i}{dt} = & [L_{i,j} + (N_{i,j,k} + N_{i,k,j})\bar{x}_k + (N_{i,j,p} + N_{i,p,j})\bar{y}_p]x'_j \\ & + [L_{i,p} + (N_{i,j,p} + N_{i,p,j})\bar{x}_j + (N_{i,j,p} + N_{i,p,j})x'_j]y'_p \\ & - (N_{i,j,p} + N_{i,p,j})\bar{x}'_j y'_p + N_{i,p,q}(y'_p y'_q - \bar{y}'_p y'_q + \bar{y}_q y'_p + \bar{y}_p y'_q) \\ & + N_{i,j,k}(x'_j x'_k - \bar{x}'_j \bar{x}'_k) + f'_i. \end{aligned} \quad (13)$$

We now define $A_{i,j} = L_{i,j} + (N_{i,j,k} + N_{i,k,j})\bar{x}_k + (N_{i,j,p} + N_{i,p,j})\bar{y}_p$, $G_{i,p} = L_{i,p} + (N_{i,j,p} + N_{i,p,j})\bar{x}_j$, $E_{i,j,p} = (N_{i,j,p} + N_{i,p,j})x'_j y'_p$, and $D_i = (N_{i,j,p} + N_{i,p,j})x'_j y'_p$. We also approximate the fast components y'_p as a white-noise vector with components η'_p and the remaining fast term $N_{i,p,q}(y'_p y'_q - \bar{y}'_p y'_q + \bar{y}_q y'_p + \bar{y}_p y'_q)$ as another white-noise forcing $B_{i,p}\zeta'_p$. Finally, neglecting the nonlinear terms $x'_j x'_k$ and $\bar{x}'_j \bar{x}'_k$, we obtain the stochastic differential equation

$$\begin{aligned} \frac{dx'_i}{dt} = & A_{i,j}x'_j + (E_{i,j,p}x'_j + G_{i,p})\eta'_p \\ & + B_{i,p}\zeta'_p - \frac{1}{2}E_{i,j,p}G_{i,p} + f'_i, \end{aligned} \quad (14)$$

which is a stochastic and linearized version of our general fluid dynamical Eq. (6). To study SSH anomalies h' ,

we can choose x'_i to be defined as h' at a given location. A detailed discussion of stochastic differential equations (SDEs) is provided by, for example, Gardiner (2004) and Kloeden and Platen (1992). See Penland (2003a,b) and Majda et al. (2008) for related discussion on climate dynamics. The SDE (14) has three noise terms: $G_{i,p}\eta'_p$ and $B_{i,p}\zeta'_p$ are additive noise terms that are uncorrelated and independent of x'_i , whereas the remaining noise term $E_{i,j,p}x'_j \eta'_p$ depends on the slowly evolving component x'_j itself and is therefore called state-dependent or multiplicative noise. Note that the additive and multiplicative noises $G_{i,p}\eta'_p$ and $E_{i,j,p}x'_j \eta'_p$ are actually correlated, because they emerge from the term $(E_{i,j,p}x'_j + G_{i,p})\eta'_p$. Therefore, this kind of stochastic forcing is called correlated additive and multiplicative (CAM) noise. The

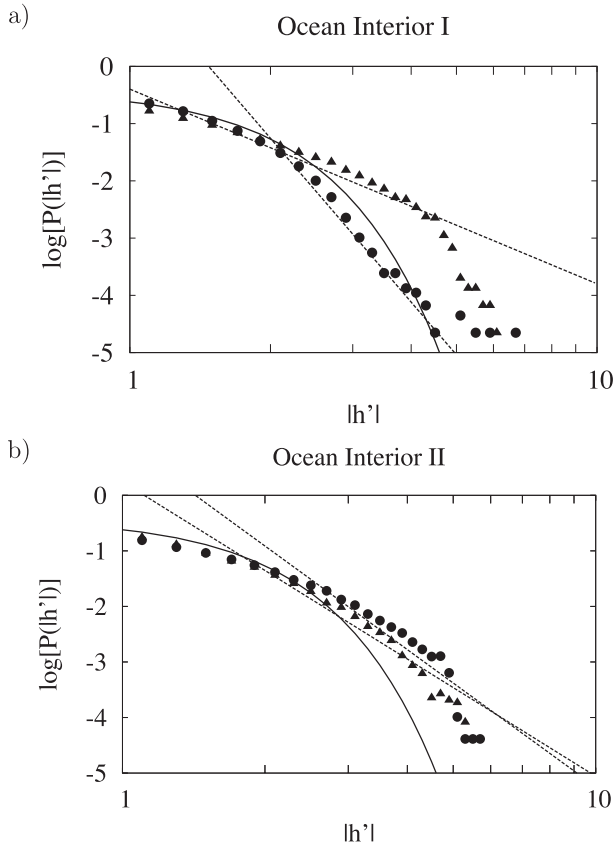


FIG. 8. Log-log scale PDFs of positive (triangles) and negative (circles) normalized SSH anomalies in the ocean interior regions: (a) 25.0° – 30.0° S, 350.0° – 360.0° E (interior I; positive skewness) and (b) 35.0° – 40.0° S, 320.0° – 330.0° E (interior II; negative skewness). The straight dashed lines are maximum likelihood estimates of the power-law behavior, and the solid lines denote Gaussian distributions.

existence of CAM in any fluid dynamical system follows naturally from the structure of the equations of motion. In other words, the evolution of quasigeostrophic (i.e., slowly varying) sea surface height anomalies h' is approximately described by an equation of type (14) with additive and multiplicative noise.

Because (14) is driven by CAM noise, it will generally have a non-Gaussian PDF, even though the deterministic part of (14) is linear [for details, see Sura and Sardeshmukh (2008), Sura (2010), and Sardeshmukh and Sura (2009)]. To understand the effect of CAM noise in more detail, we will briefly discuss the behavior of the univariate version of (14), neglecting the external forcing f' . Note that this does not mean we directly derive a univariate approximation of (14) mathematically. This cannot be done in a mathematically straightforward way, but the parameters can be potentially derived from data. The one-dimensional system is just the simplest, mathematically tractable CAM noise equation that, however,

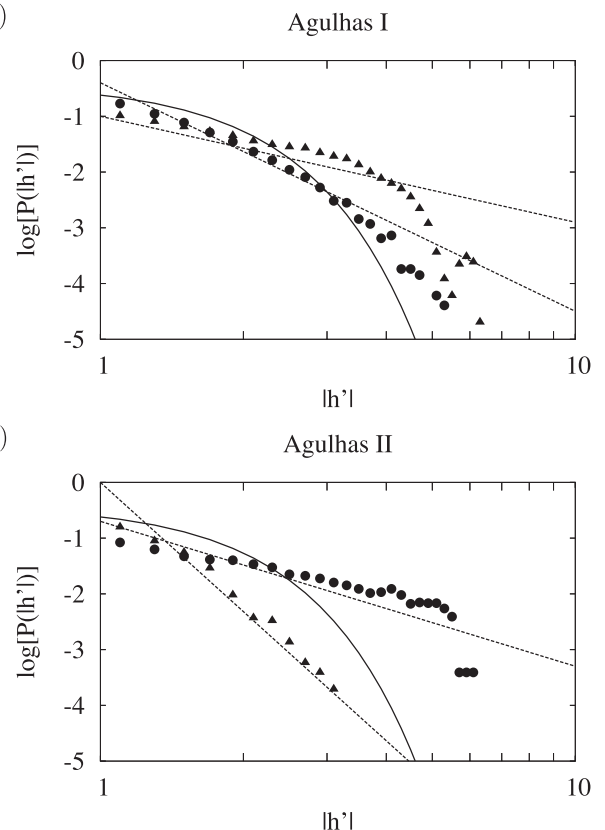


FIG. 9. As in Fig. 8, but for the Agulhas regions: (a) 40.0° – 45.0° S, 10.0° – 20.0° E (Agulhas I; positive skewness) and (b) 34.8° – 36.5° S, 23.0° – 26.1° E (Agulhas II; negative skewness).

governs the higher-order statistics of the general multivariate system remarkably well (the reasons for that are discussed later). Dropping the primes for the sake of convenience, the one-dimensional equation may be written as

$$\frac{dx}{dt} = Ax + (Ex + G)\eta - \frac{1}{2}EG + B\zeta, \quad (15)$$

where A , E , G , and B are now scalar constants (not directly related to their multivariate counterparts $A_{i,j}$, $E_{i,j,p}$, $G_{i,p}$, and $B_{i,p}$ earlier) and η and ζ are scalar Gaussian white-noise processes with unit variance. [So far we have not come up with a stable and reliable method to estimate all parameters of the multiplicative noise SDE (15) from relatively short records. In general, it is nontrivial to estimate coefficients of SDEs from limited data (e.g., Kloeden and Platen 1992; Sura and Barsugli 2002).] As shown in detail by Sura and Sardeshmukh (2008) and Sardeshmukh and Sura (2009), the PDF $P(x)$ and equations for the moments can be obtained from the Fokker–Planck equation corresponding to (15). Here, we omit the

mathematical derivations and go on to present the main results. The most relevant results are that a variable x governed by (15) has

- the property that the (excess) kurtosis K is always greater than 1.5 times the square of the skewness S , $K \geq 1.5 S^2$, and
- a PDF with power-law tails, $P(x) \propto x^{-\alpha}$.

The K - S inequality and the power-law behavior are consistent with observed non-Gaussian variability of SSTs (Sura and Sardeshmukh 2008; Sura 2010) and non-Gaussian atmospheric geopotential height and vorticity variability (Sardeshmukh and Sura 2009). Note, however, that in the atmospheric case we also observe a slight vertical offset of the parabola. That is, for atmospheric geopotential height and vorticity variability, we have $K \geq 1.5S^2 - r$, with $r = 0.6$. The dynamical reason for the offset is discussed later.

The empirical results of section 2 showed that, for SSH anomalies, $K \geq 1.5S^2 - 1.5$ (Fig. 3). The 1.5 factor (multiplying S^2) does not appear in any standard unimodal distribution, and it is most likely a signature of multiplicative noise dynamics. We are not aware of another dynamical mechanism capable of producing the constraint $K \geq 1.5S^2 - 1.5$ and power-law statistics.

Therefore, a SDE of type (14) is a prime candidate to explain the statistics of non-Gaussian SSH anomalies from first dynamical principles. What remains to be explained is why the local univariate model (15) is also successful in explaining the essential character (power law and K - S relationship with offset) of observed non-Gaussian variability in the ocean, where nonlocal, multivariate dynamics are obviously important. The key point, however, is that this success applies to the understanding and simulation of the higher-order non-Gaussian statistics and power-law tails, not to lower-order statistics such as variance. How can we understand this behavior?

Sardeshmukh and Sura (2009) showed that the one-dimensional model (15) becomes progressively better at representing higher-order statistics of multivariate systems through a principle of increasing “diagonal dominance” in the higher-order moment equations. Diagonal dominance refers to the progressively greater importance of the self-correlation terms in the higher-order moment equations of multivariate systems. This diagonal dominance is thus the basic reason for the relevance of the one-dimensional model (15) in the dynamics of the higher-order moments, even in multivariate systems.

The fact that the higher-order moment equations are more diagonally dominant also helps explain this vertical offset relative to the prediction of the one-dimensional theory. The key to understanding this qualitatively is to recognize that diagonal dominance is stronger for

the higher moments. That is, the error we make using a one-dimensional system to approximate a multivariate system is largest for the second moment (the mean is zero by construction of our anomaly equations) and successively smaller for the higher moments. In addition, because the multivariate system has larger variance, we know the sign of the error we make in the second moments by using a univariate system to approximate a multivariate system. This relies on the fact that a linear operator A is in almost all geophysical contexts a “non-normal” operator³ that does not commute with its transpose. This nonnormality of the linear dynamical system leads to a greater variance of x than for a “normal” A with the same eigenvalues (Ioannou 1995); a one-dimensional system is, of course, always normal. In most cases, this nonnormality is associated with the ability of anomalies to draw energy from a background state, of which there is pervasive evidence and which is indeed one of the cornerstones of dynamical meteorology and oceanography. Now it can be seen from the definition of kurtosis, $K = x'^4/\sigma^4 - 3$, that an increased variance in combination with a negligible error in the fourth moment will lead to a decrease of K : the parabola is effectively shifted downward. Therefore, the multivariate system results in an inequality $K \geq 1.5S^2 - r$, with a small positive constant r . Details can be found in Sardeshmukh and Sura (2009).

To summarize, we have strong observational evidence, both from the skewness–kurtosis link and from the power-law scaling, that the stochastic and linearized version (14) of the general fluid dynamical Eq. (6) is an appropriate first-order approximation to explain non-Gaussian SSH variability. This is a significant step beyond the important but mainly empirical studies by previous investigators (e.g., Thompson and Demirov 2006). The knowledge of the type of SDE that governs SSH variability will potentially allow us to study the (statistical) dynamics of SSH anomalies in more detail and might reveal more relevant features of related geostrophic turbulence. In fact, analytical predictions of higher-order statistics and comparison of such theory with observations are in the best tradition of probing deeply into turbulence. On the more applied side, the analytically derived skewness–kurtosis link has the potential to serve as a metric for assessing the performance of numerical ocean models. For example, a model that in some way suppressed the correlated effects of additive and multiplicative noise would be expected to show a skewness–kurtosis relationship that differed from that in observations.

³ Here, nonnormal refers to the nonorthogonality of the eigenfunctions of A and should not be confused with non-Gaussianity.

4. Summary and discussion

This study has applied stochastic theory to altimetric measurements of sea surface height specifically to examine the relationship between skewness and kurtosis and, more generally, the physical origin of non-Gaussian (extreme) sea surface variations. Some statistics (skewness) of non-Gaussian SSH variability are already documented (Thompson and Demirov 2006). Here, we have provided a more quantitative analysis, studying non-Gaussian sea surface height variability in a stochastic dynamical framework. For SSH anomalies, excess kurtosis is equal to or larger than 1.5 times the squared skewness (minus an adjustment constant). Because there is no obvious dynamical reason why sea surface height variability should behave this way, the observed link itself is a remarkable finding. We employed a general stochastic dynamical theory derived from first dynamical principles (Sura and Sardeshmukh 2008; Sardeshmukh and Sura 2009) that explains the observed link between SSH skewness and kurtosis. To that extent, we can attribute the non-Gaussian statistics of SSH variability to a correlated additive and multiplicative noise forcing. This kind of forcing naturally appears in the equations of motion through a fast–slow time-scale separation. That is, the observed skewness–kurtosis link serves as one point of observational evidence that the assumption of the time-scale separation is at least approximately valid for the oceanic SSH field. The theory is also consistent with observed power-law PDF tails.

In general, we conclude that non-Gaussian behavior is an inherent property of geophysical flows, and stochastic theory provides an appropriate tool to model the dynamics of extreme events in geophysical systems. We also note that multiplicative stochastic forcing is equivalent to a non-Gaussian closure of the moment hierarchy in a turbulent fluid. The multiplicative noise approach might provide guidance to develop new turbulence closure schemes. Additive noise is already used to close the lower-order moment hierarchy in turbulence (e.g., Salmon 1998). Our results clearly show that multiplicative noise has the potential to provide higher-order closures in geophysical fluid dynamics.

Perhaps the most important and specific result from our analysis is that we can attribute non-Gaussian SSH variability to stochastically forced linear dynamics. In fact, we are not currently aware of a simple nonlinear model with the same ability to explain the observed skewness–kurtosis link. This has important implications with respect to understanding SSH variability. For example, our study raises the possibility of predicting probabilities of extreme sea surface height anomalies from first physical principles and may provide a useful

null hypothesis for non-Gaussian sea surface height variability. Such a null hypothesis is needed to test if an observed sea level rise or storm surge is due to a trend or natural non-Gaussian variability. The results also show that regions with low values of kurtosis—the Gulf Stream, the Kuroshio Extension, the Agulhas Retroflection, the Gulf of Mexico Loop Current, and perhaps the eastern tropical Pacific—correspond to regions with bimodal sea surface height PDFs. Comparing kurtosis against squared skewness thus can serve as a simple test to identify regions of the ocean with prominent bimodal patterns of variability. On the modeling side, the specific skewness–kurtosis relationship observed here also sets a clear standard that can be used to evaluate the performance of ocean circulation models and to further probe variability in upper-ocean processes.

The work in this paper evaluates PDFs from altimetry and their skewness and kurtosis by assuming random forcing, where the sole source of non-Gaussianity is the state-dependent character of the atmospheric noise forcing. In reality, we have considerable knowledge of the wind stress and air-sea fluxes that drive the ocean, and this suggests that the theory presented here could eventually be refined to account for the known character of oceanic forcing.

Acknowledgments. We thank two anonymous reviewers for their valuable comments that led to significant improvements of the original manuscript. The altimeter products were produced by SSALTO/DUACS and distributed by AVISO with support from the Centre National d'Etudes Spatiales (CNES). The along-track sea level anomaly data used in this study are available online (<ftp://ftp.cls.fr/pub/oceano/AVISO/SSH/duacs/global/dt/ref/sla/tp/>). Author PS was partly supported by NSF Grant ATM-0552047. STG acknowledges support from the National Aeronautics and Space Administration through the Ocean Surface Topography Science Working Team, JPL Contract 1224031.

APPENDIX

Estimating Power Laws from Data

In this appendix, we briefly review how to estimate power laws [i.e., a PDF $P(x) \propto x^{-\alpha}$ with the exponent α] from data. More comprehensive discussions may be found in many textbooks and papers (e.g., Sornette 2006; Newman 2005; Clauset et al. 2009).

The best-fit (i.e., maximum likelihood) power-law exponent α for a general positive time series x_i of length n is

$$\alpha = 1 + n \left[\sum_{i=1}^n \ln\left(\frac{x_i}{x_{\min}}\right) \right]^{-1}, \quad (\text{A1})$$

where x_{\min} is the lower bound of the power-law behavior. Note that the general description in (A1) requires x_i and x_{\min} to be positive and therefore not directly applicable to sea surface height (SSH) anomalies h' . Hence, (A1) has to be applied separately to the absolute values of $|h'|$ for positive and negative perturbations (however, for the sake of simplicity, we keep the general terminology, x_i and x_{\min}). The approximate standard error ϵ of α can be derived from the width of the likelihood maximum as

$$\epsilon = \frac{\alpha - 1}{\sqrt{N_{\text{in}}}}, \quad (\text{A2})$$

where N_{in} is the effective number of independent observations. For example, the interval $\alpha \pm 1.96\epsilon$ contains the true power-law exponent with approximately 95% certainty.

The term x_{\min} is chosen to make the PDF of the observed data and the best-fit power-law model as similar as possible above x_{\min} (Clauset et al. 2009). As a measure for quantifying the distance between two PDFs, the Kolmogorov–Smirnov statistic \mathcal{D} (e.g., Wilks 2006; Press et al. 1992) is used. Here, \mathcal{D} is simply the maximum distance between the cumulative density function (CDF) of the data and the best-fit model:

$$\mathcal{D} = \max_{x \geq x_{\min}} |S(x) - P(x)|, \quad (\text{A3})$$

where $S(x)$ is the CDF of the data above x_{\min} and $P(x)$ is the CDF of the best-fit power-law model above x_{\min} . The best estimate of x_{\min} is the value that minimizes \mathcal{D} . It is also straightforward to use Kolmogorov–Smirnov statistics to test if the observed data are consistent with a power-law distribution; that is, to perform a goodness-of-fit test. This can be done using a Monte Carlo approach. First, the power-law exponent α and the cutoff x_{\min} are calculated from the data. The goodness of fit to the data is quantified by the Kolmogorov–Smirnov distance \mathcal{D} . Then, using the observed parameters, a large ensemble of synthetic power-law time series of length N_{in} are generated and the power-law exponent α , lower-bound x_{\min} , and Kolmogorov–Smirnov distance \mathcal{D} (now from its known CDF) are estimated for each of them employing the techniques described earlier. Finally, the fraction of the Kolmogorov–Smirnov statistics for the synthetic datasets whose value exceed the statistics of the real data yields the so-called p value. Only if the

p value is sufficiently small can a power-law distribution be ruled out. Note that we use Kolmogorov–Smirnov statistics and the related p value to reject (rather than confirm) a hypothesis for the observed data; hence, high p values, not low ones, are considered good. Here, a power law is ruled out if $p \leq 0.1$. That is, if $p \leq 0.1$, there is a 10% or less probability to draw a power-law sample merely by chance that agrees that poorly with power-law statistics, and the hypothesis that the data are drawn from a power law is rejected.

REFERENCES

- Bane, J. M., Jr., and W. K. Dewar, 1988: Gulf Stream bimodality and variability downstream of the Charleston Bump. *J. Geophys. Res.*, **93**, 6695–6710.
- Bracco, A., J. H. LaCasce, and A. Provenzale, 2000: Velocity probability density functions for oceanic floats. *J. Phys. Oceanogr.*, **30**, 461–474.
- Brooks, C. E. P., and N. Carruthers, 1953: *Handbook of Statistical Methods in Meteorology*. Her Majesty's Stationery Office, 412 pp.
- Chao, S.-Y., 1984: Bimodality of the Kuroshio. *J. Phys. Oceanogr.*, **14**, 92–103.
- Clauset, A., C. R. Shalizi, and M. E. J. Newman, 2009: Power-law distributions in empirical data. *SIAM Rev.*, **51**, 661–703.
- Dong, S., and K. A. Kelly, 2004: Heat budget in the Gulf Stream region: The importance of heat storage and advection. *J. Phys. Oceanogr.*, **34**, 1214–1231.
- Ducet, N., P. Y. L. Traon, and G. Reverdin, 2000: Global high-resolution mapping of ocean circulation from the combination of TOPEX/Poseidon and ERS-1 and -2. *J. Geophys. Res.*, **105**, 19 477–19 498.
- Gardiner, C. W., 2004: *Handbook of Stochastic Methods for Physics, Chemistry and the Natural Science*. 3rd ed. Springer-Verlag, 415 pp.
- Gille, S. T., 2004: Using Kolmogorov–Smirnov statistics to assess Jason, TOPEX, and Poseidon altimeter measurements. *Mar. Geod.*, **27** (1–2), 47–58.
- , and S. G. Llewellyn Smith, 2000: Velocity-variance probability distribution functions from altimeter measurements. *J. Phys. Oceanogr.*, **30**, 125–136.
- Hasselmann, K., 1976: Stochastic climate models. Part I. Theory. *Tellus*, **28**, 473–484.
- Hughes, C. W., A. F. Thompson, and C. Wilson, 2010: Identification of jets and mixing barriers from sea level and vorticity measurements using simple statistics. *Ocean Modell.*, **32**, 44–57, doi:10.1016/j.ocemod.2009.10.004.
- Ioannou, P. J., 1995: Nonnormality increases variance. *J. Atmos. Sci.*, **52**, 1155–1158.
- Isern-Fontanet, J., E. García-Ladona, J. Font, and A. García-Olivares, 2006: Non-Gaussian velocity probability density functions: An altimetric perspective of the Mediterranean Sea. *J. Phys. Oceanogr.*, **36**, 2153–2164.
- , G. Lapeyre, P. Klein, B. Chapron, and M. W. Hecht, 2008: Three-dimensional reconstruction of oceanic mesoscale currents from surface information. *J. Geophys. Res.*, **113**, C09005, doi:10.1029/2007JC004692.
- Klaassen, C. A. J., P. J. Mokveld, and B. van Es, 2000: Squared skewness minus kurtosis bounded by 186/125 for unimodal distributions. *Stat. Probab. Lett.*, **50**, 131–135.

- Kloeden, P., and E. Platen, 1992: *Numerical Solution of Stochastic Differential Equations*. Springer-Verlag, 632 pp.
- LaCasce, J. H., 2005: Eulerian and Lagrangian velocity distributions in the North Atlantic. *J. Phys. Oceanogr.*, **35**, 2327–2336.
- Lapeyre, G., and P. Klein, 2006: Dynamics of the upper oceanic layers in terms of surface quasigeostrophic theory. *J. Phys. Oceanogr.*, **36**, 165–176.
- Llewellyn Smith, S. G., and S. T. Gille, 1998: Velocity probability density functions of large-scale turbulence in the upper ocean. *Phys. Rev. Lett.*, **81**, 5249–5252.
- Lynch, P., 2006: *The Emergence of Numerical Weather Prediction: Richardson's Dream*. Cambridge University Press, 279 pp.
- Majda, A. J., C. Franzke, and B. Khouider, 2008: An applied mathematics perspective on stochastic modelling for climate. *Philos. Trans.*, **366**, 2429–2455.
- Maul, G. A., and F. M. Vukovich, 1993: The relationship between variations in the Gulf of Mexico Loop Current and Straits of Florida volume transport. *J. Phys. Oceanogr.*, **23**, 785–796.
- Monahan, A. H., 2004: A simple model for the skewness of global sea-surface winds. *J. Atmos. Sci.*, **61**, 2037–2049.
- , 2006a: The probability distributions of sea surface wind speeds. Part I: Theory and SSM/I observations. *J. Climate*, **19**, 497–520.
- , 2006b: The probability distributions of sea surface wind speeds. Part II: Dataset intercomparison and seasonal variability. *J. Climate*, **19**, 521–534.
- Newman, M. E. J., 2005: Power laws, Pareto distributions and Zipf's law. *Contemp. Phys.*, **46**, 323–351.
- Pedlosky, J., 1987: *Geophysical Fluid Dynamics*. 2nd ed. Springer-Verlag, 710 pp.
- Peinke, J., F. Böttcher, and S. Barth, 2004: Anomalous statistics in turbulence, financial markets and other complex systems. *Ann. Phys.*, **13**, 450–460.
- Penland, C., 2003a: Noise out of chaos and why it won't go away. *Bull. Amer. Meteor. Soc.*, **84**, 921–925.
- , 2003b: A stochastic approach to nonlinear dynamics: A review (extended version of the article "Noise out of chaos and why it won't go away"). *Bull. Amer. Meteor. Soc.*, **84**, ES43–ES51.
- Press, W. H., S. A. Teukolsky, W. T. Vetterling, and B. P. Flannery, 1992: *Numerical Recipes in Fortran, The Art of Scientific Computing*. Cambridge University Press, 963 pp.
- Qiu, B., and W. Miao, 2000: Kuroshio path variations south of Japan: Bimodality as a self-sustained internal oscillation. *J. Phys. Oceanogr.*, **30**, 2124–2137.
- Reynolds, R. W., T. M. Smith, C. Liu, D. B. Chelton, K. S. Casey, and M. G. Schlax, 2007: Daily high-resolution blended analyses for sea surface temperature. *J. Climate*, **20**, 5473–5496.
- Salmon, R., 1998: *Lectures on Geophysical Fluid Dynamics*. Oxford University Press, 378 pp.
- Sardeshmukh, P. D., and P. Sura, 2009: Reconciling non-Gaussian climate statistics with linear dynamics. *J. Climate*, **22**, 1193–1207.
- Schmeits, M. J., and H. A. Dijkstra, 2001: Bimodal behavior of the Kuroshio and the Gulf Stream. *J. Phys. Oceanogr.*, **31**, 3435–3456.
- Sornette, D., 2006: *Critical Phenomena in Natural Sciences*. Springer, 528 pp.
- Sturges, W., and R. Leben, 2000: Frequency of ring separations from the Loop Current in the Gulf of Mexico: A revised estimate. *J. Phys. Oceanogr.*, **30**, 1814–1819.
- Sura, P., 2003: Stochastic analysis of Southern and Pacific Ocean sea surface winds. *J. Atmos. Sci.*, **60**, 654–666.
- , 2010: On non-Gaussian SST variability in the gulf stream and other strong currents. *Ocean Dyn.*, **60**, doi:10.1007/s10236-009-0255-9.
- , and J. J. Barsugli, 2002: A note on estimating drift and diffusion parameters from timeseries. *Phys. Lett.*, **305A**, 304–311.
- , and S. T. Gille, 2003: Interpreting wind-driven Southern Ocean variability in a stochastic framework. *J. Mar. Res.*, **61**, 313–334.
- , and M. Newman, 2008: The impact of rapid wind variability upon air-sea thermal coupling. *J. Climate*, **21**, 621–637.
- , and P. D. Sardeshmukh, 2008: A global view of non-Gaussian SST variability. *J. Phys. Oceanogr.*, **38**, 639–647.
- , M. Newman, C. Penland, and P. D. Sardeshmukh, 2005: Multiplicative noise and non-Gaussianity: A paradigm for atmospheric regimes? *J. Atmos. Sci.*, **62**, 1391–1409.
- , —, and M. A. Alexander, 2006: Daily to decadal sea surface temperature variability driven by state-dependent stochastic heat fluxes. *J. Phys. Oceanogr.*, **36**, 1940–1958.
- Thompson, K. R., and E. Demirov, 2006: Skewness of sea level variability of the world's oceans. *J. Geophys. Res.*, **111**, C05005, doi:10.1029/2004JC002839.
- Wilkins, J. E., 1944: A note on skewness and kurtosis. *Ann. Math. Stat.*, **15**, 333–335.
- Wilks, D. S., 2006: *Statistical Methods in the Atmospheric Sciences*. 2nd ed. Academic Press, 627 pp.